Anisotropic anharmonicity dictates the thermal conductivity of β-Ga_2O_3

Abdulaziz Alkandari,[1,2] Zherui Han,[1] Ziqi Guo,[1] Thomas E. Beechem,[1,*] and Xiulin Ruan[1,†]
[1]*School of Mechanical Engineering and Birck Nanotechnology Center, Purdue University, West Lafayette, 47907 Indiana, USA*
[2]*Mechanical Engineering Department, College of Engineering and Petroleum, Kuwait University, PO Box 5969, Safat 13060, Kuwait*

(Received 16 October 2024; revised 10 February 2025; accepted 6 March 2025; published 20 March 2025)

β-Ga_2O_3 is a promising material candidate for next-generation high-power devices even as its low thermal conductivity (κ) limits utilization due to an inability to sufficiently dissipate heat. Despite the importance of this inherent thermal challenge, a significant discrepancy persists between experimental results and computational models regarding the anisotropic thermal conductivity of β-Ga_2O_3. Specifically, computational results are within experimental error bounds for κ_{100} and κ_{001} while underpredicting κ_{010}, suggesting that the bare phonon models used in the literature are missing essential physics related to the anisotropic thermal transport. In response, we compute the anisotropic κ using first principles and the Peirels-Boltzmann transport equation under different approximations. For the simplest model, we consider the heat carriers to be harmonic phonons with scattering rates obtained perturbatively. These results are then compared with those obtained by including phonon renormalization and four-phonon scattering. Our results show that accounting for phonon renormalization resolves the discrepancy between experiment and theory. This is because phonon renormalization leads to an anisotropic κ enhancement caused by directionally dependent changes in the phonon group velocities accompanied by a general increase in phonon lifetime. Owing to the crucial role of these anharmonic interactions in accurately describing anisotropic thermal transport, we also explore the anharmonicity of individual atoms and show that the octahedrally coordinated gallium atom is the most anharmonic and thus most likely responsible for the failure of the harmonic phonon model to describe thermal transport in this material. Finally, we demonstrate that atomic anharmonicities could be used as a useful metric to guide the tailoring of vibrational properties.

DOI: 10.1103/PhysRevB.111.094308

I. INTRODUCTION

Ultrawide-band-gap (>3.4 eV) semiconductors have reached a technological maturity in which the fundamental potential has motivated significant effort to pursue commercial adoption [1]. Since the breakdown voltage increases nonlinearly with the band gap, ultrawide-band-gap materials are promising candidates for robust power device performance at high voltages and temperatures [2]. To capitalize on this potential, fundamental understanding of the material physics in those regimes must be known. There remain, however, knowledge gaps regarding even intrinsic material properties like thermal conductivity in these materials [3,4]. With this motivation, we examine here the magnitude and underlying mechanisms belying the highly anisotropic nature of thermal conductivity in β-Ga_2O_3.

β-Ga_2O_3 is an ultrawide-band-gap (4.8 eV) [5] material that is commercially available in high-quality wafers produced using inexpensive melt growth processes [6]. This allows β-Ga_2O_3 power devices to be more economically viable than other wide-band-gap materials such as SiC and GaN [7]. However, the thermal conductivity (κ) of β-Ga_2O_3 is very low (11–27 W m^{-1} K^{-1}) [8] when compared with these materials ($\kappa_{SiC} \approx 500$ W m^{-1} K^{-1} [9], $\kappa_{GaN} \approx 230$ W m^{-1} K^{-1} [10]). The low κ necessitates more aggressive thermal management schemes, such as double-side cooling [11]. Therefore, thermal management is one of the significant barriers toward commercialization of β-Ga_2O_3 electronics. A robust understanding of its intrinsic thermal transport properties is, therefore, warranted.

β-Ga_2O_3 has a monoclinic crystal structure, as shown in Fig. 1, leading to four independent components of the thermal conductivity tensor [12]. The crystal structure is also highly anisotropic ($a = 12.214$ Å, $b = 3.0371$ Å, $c = 5.7981$ Å, and $\beta = 103.83°$) [13], causing significant anisotropy in the measured thermal conductivity ($\kappa_{100} = 9.5$–18 W m^{-1} K^{-1}, $\kappa_{010} = 22.5$–29.0 W m^{-1} K^{-1}, and $\kappa_{001} = 12.7$–21.0 W m^{-1} K^{-1}) [8,14–17]. The highly anisotropic thermal conductivity of β-Ga_2O_3 differentiates it from other ultrawide-band-gap materials like GaN that effectively transports heat isotropically despite possessing a thermal conductivity tensor that is formally anisotropic [18].

The thermal conductivity of β-Ga_2O_3 has been extensively studied both experimentally [8,14–17] and computationally [19,20]. However, discrepancies exist between the computational and experimental thermal conductivities. Specifically, the computational results are within experimental error bounds for κ_{100} and κ_{001} while under-predicting κ_{010} ($\approx$ 4–32%). This peculiar mismatch suggests that computational models may be missing important physics relevant to the anisotropic thermal transport in β-Ga_2O_3.

The combination of density functional theory (DFT) and the Peirels-Boltzmann transport equation (PBTE) has led to a framework capable of predicting thermal transport in solids

*Contact author: tbeechem@purdue.edu
†Contact author: ruan@purdue.edu

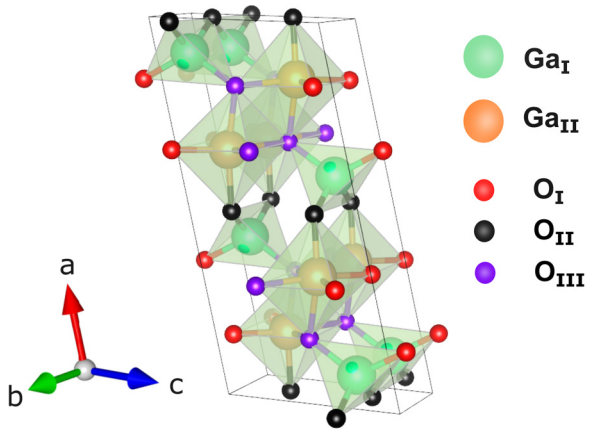

FIG. 1. Conventional unit cell of monoclinic β-Ga_2O_3. The unit cell contains 20 atoms with five crystallographically nonequivalent atoms. One gallium atom is tetrahedrally coordinated (Ga_I), while the other is octahedrally coordinated (Ga_{II}). The three remaining oxygen atoms sit between the polyhedra: (O_I) is at the corner of two octahedra and one tetrahedron, (O_{II}) is at the corner of two tetrahedra and one octahedron, and (O) is at the corner of three octahedra and one tetrahedron [13].

with high accuracy [21]. However, differences between the experimentally measured κ and those obtained from the standard computational workflow (described in detail in Ref. [22]) exist when the assumptions inherent to the predictions conflict with the reality of the system under study. More simply, discrepancies between experiment and theory happen when assumptions break down. It is, therefore, necessary to consider the assumptions underlying predictions of the anisotropic thermal conductivity in β-Ga_2O_3.

For β-Ga_2O_3, the standard PBTE method, which presumes that the phonons are well-defined quasiparticles, is valid. This assumption is justified if the phonon mean free paths are reasonably larger than the interatomic spacing or if the phonon lifetimes are greater than the inverse frequency of the phonon mode [23]. For β-Ga_2O_3, experimental measurements of the phonon lifetimes [24] are consistent with this picture. In addition, β-Ga_2O_3 exhibits an appreciably larger thermal conductivity relative to materials where the formalism is known to break down [25]. Taken together, the phonon quasiparticle picture is reasonable to use with β-Ga_2O_3, and hence, the PBTE is valid. More recently, coherent (interband) contributions to the lattice thermal conductivity have been shown to be crucial for strongly anharmonic solids [26–34]. In these materials, the phonon particlelike (intraband) thermal conductivity typically lies <1 W m^{-1} K^{-1}, and the interband channel ($\leqslant$0.4 W m^{-1} K^{-1}) thus becomes significant. In contrast, for β-Ga_2O_3, the intraband conductivity exceeds these values by more than an order of magnitude, making any interband contribution comparatively negligible. Consequently, using the standard Peierls-Boltzmann approach should be sufficient to capture both the overall magnitude and the anisotropy of the thermal conductivity of β-Ga_2O_3. Therefore, we turn our attention to the approximations introduced by DFT and the difficulties that come about when using it to accurately predict thermal conductivity along all directions in β-Ga_2O_3.

Defects are an obvious candidate. Standard DFT approaches employ periodic boundary conditions where the crystal structure is assumed to be defect free. This is in contrast with the imperfections that exist in almost every real-world material. Defects are not, however, the chief cause here. For example, although neglecting phonon-defect scattering may explain why κ is overpredicted in two crystal directions (e.g., κ_{100} and κ_{001}), thermal conductivity is underpredicted along the κ_{010} direction. It seems very unlikely that defects would mitigate transport along two directions while boosting it along the third.

Instead, attention is turned to the role of anharmonicity on anisotropic thermal transport. DFT is an inherently ground-state approach [35]. This limits any perturbative treatment of the lattice potential energy expansion terms to be temperature independent. Therefore, obtaining the phonon energies from the Hessian matrix of the expansion, known as the harmonic approximation, leads to phonon energies that are also temperature independent [36]. The finite-temperature effects on the potential energy expansion terms—and hence on the phonon energies and even the atomic displacement themselves (i.e., polarizations)—are known as phonon renormalization effects. The extent to which these effects impact κ in β-Ga_2O_3 in general and along different crystal in particular is unknown. Therefore, we focus on anharmonicity and how it manifests specifically in the thermal transport of β-Ga_2O_3.

Phonon renormalization effects are negligible for κ at room temperature in strongly bonded solids such as silicon, diamond, and MgO [37,38]. However, they are crucial for accurate prediction of κ in other solids such as NaCl [37], PbTe [39], and a wide range of oxides including TiO_2 [40], $SrTiO_3$ [41], and CeO_2 [38]. Accounting for phonon renormalization in the calculation of κ in TiO_2, for example, leads to a 50% increase at room temperature and significantly better agreement with experimental data [40]. Therefore, phonon renormalization could play a significant role in determining the thermal conductivity of β-Ga_2O_3 and, if ignored, lead to discrepancies between experiment and prediction.

Similarly, four-phonon (4ph) scattering may also be significant, requiring its assessment as well. Higher-order phonon scattering can significantly reduce κ [42–46], especially in materials whose optical phonons significantly contribute to the thermal transport [44]. Authors of previous work have suggested that optical phonon modes contribute $>$50% to κ_{010} in β-Ga_2O_3 [19]. Recognizing this, we examine here the the net interplay between phonon renormalization and 4ph scattering and its impact on the anisotropic response of thermal conductivity in β-Ga_2O_3.

Specifically, we combine a self-consistent phonon framework with a solution of the PBTE to include phonon renormalization, thermal expansion, and 4ph scattering to calculate κ of β-Ga_2O_3 in the temperature range between 200 and 600 K. The upper limit of this range corresponds to the operational temperature in electric vehicles, where the temperature near the engine can reach up to 200 °C [47]. We observe that including phonon renormalization resolves the discrepancy between experimental and computational κ in β-Ga_2O_3. The κ enhancement due to renormalization is anisotropic and highest for κ_{010}, the same tensor element that was significantly underpredicted by previous computational

studies. Furthermore, we show that 4ph scattering is weak relative to the dominant three-phonon (3ph) scattering in this temperature range. By quantifying the anharmonicity of the individual atoms, we discover that the motion of the octahedrally coordinated gallium atom (Ga_{II}) is the most sensitive to the temperature-dependent potential energy surface (i.e., is the most anharmonic). Practically, this suggests that enhancing κ of β-Ga_2O_3 could be achieved by alloying with an element that takes the Ga position in the crystal structure.

II. METHODOLOGY

In this section, we elaborate on our workflow to calculate κ of β-Ga_2O_3 using a first-principles approach. From a solution of the PBTE for the phonon equilibrium distribution function f_λ, the thermal conductivity tensor [48] is expressed as

$$\kappa^{\alpha\beta} = \frac{1}{k_B T^2 NV} \sum_\lambda (\hbar\omega_\lambda)^2 f_\lambda^0 \left(f_\lambda^0 + 1\right) \mathbf{v}_\lambda^\alpha \mathbf{v}_\lambda^\beta \tau_\lambda, \tag{1}$$

where λ is a phonon mode index including the polarization and wave vector, α and β are Cartesian directions, k_B is the Boltzmann constant, T is the temperature, N is the number of unit cells, V is the volume of the unit cell, $\hbar$ is the reduced Planck constant, ω_λ is the mode frequency, $\mathbf{v}_\lambda$ is the mode group velocity, and τ_λ is the mode lifetime. Therefore, the evaluation of κ requires knowledge of the energy carrier (phonon) velocities and lifetimes.

These velocities and lifetimes are obtained from DFT using either the ground-state (standard approach) or from a finite-temperature (effective) potential energy surface (PES). To understand this in more detail, we begin by writing the Taylor expansion of the lattice potential energy (U) about the equilibrium position of the atoms

$$U = U_0 + \frac{1}{2!}\sum_{ij} \frac{\partial^2 U}{\partial \mathbf{u}_i \partial \mathbf{u}_j} \mathbf{u}_i \mathbf{u}_j + \frac{1}{3!}\sum_{ijk} \frac{\partial^3 U}{\partial \mathbf{u}_i \partial \mathbf{u}_j \partial \mathbf{u}_k} \mathbf{u}_i \mathbf{u}_j \mathbf{u}_k + \frac{1}{4!}\sum_{ijkl} \frac{\partial^4 U}{\partial \mathbf{u}_i \partial \mathbf{u}_j \partial \mathbf{u}_k \partial \mathbf{u}_l} \mathbf{u}_i \mathbf{u}_j \mathbf{u}_k \mathbf{u}_l + \ldots, \tag{2}$$

where U_0 is the energy at the equilibrium position, $\mathbf{u}_i$ represents the displacement of atom i from its equilibrium position, and the derivatives represent increasing orders of interatomic force constants (IFCs). The second-order IFC (Hessian) is used to calculate the phonon dispersion and therefore velocities. This is done by diagonalization of the dynamical matrix assembled from the mass-normalized Hessian. The higher-order IFCs are needed to calculate the 3ph and 4ph scattering rates.

Terminating the expansion at the Hessian is known as the harmonic approximation. In this approximation, the lattice energy can be written as a sum of noninteracting normal modes. This assumption is necessary to obtain the phonon energies, as including higher-order IFC into the lattice potential energy no longer leads to a diagonalizable dynamical matrix. This makes accounting for anharmonicity in the phonon energies (i.e., phonon renormalization) problematic. The temperature-dependent effective potential (TDEP) accomplishes this task by introducing model IFCs that represent an effective PES [like Eq. (2)]. This effectively maps the effect of phonon anharmonicity onto the model Hessian. This model Hessian can be diagonalized to obtain the phonon energies renormalized by phonon anharmonicity, leading to temperature-dependent phonon energies. To do this, TDEP constructs the model Hessian and the higher-order IFCs by minimizing the difference between the model forces and force-displacement datasets.

In this paper, we utilize the stochastic TDEP (s-TDEP) [49–52] to extract the renormalized Hessian and higher-order IFCs. The s-TDEP method is based on stochastic generation of atomic thermal displacements followed by fitting force-displacement datasets to a model Hamiltonian [53]. Therefore, s-TDEP allows extracting the temperature-dependent PES, up to fourth-order terms and including zero-point quantum motion, at a reasonable computational cost compared with *ab initio* molecular dynamics (AIMD). In the TDEP approach, the IFCs are fit in ascending order, ensuring that the second-order IFCs are the largest. This implies that the second-order IFCs are renormalized to infinite order. The higher-order IFCs are then fit from the residual forces. This ensures that there is no double-counting of the anharmonicity in the higher-order IFCs [37,54,55]. Up to this point, we showed how to obtain the phonon energies using either the ground-state Hessian, obtained directly from DFT, or from the temperature-dependent Hessian constructed by TDEP. The final task is to lay the theory necessary to calculate the total phonon scattering rates.

Using the third- and fourth-order IFCs, the 3ph and 4ph scattering rates can be evaluated using Fermi's golden rule [48]. In this paper, isotopic scattering is neglected to focus exclusively on the intrinsic phonon scattering mechanisms arising from the anharmonicity of the material. To obtain the total scattering rate, Mattheisen's rule is employed to sum all the contributions from the individual scattering channels [48,56,57]:

$$\frac{1}{\tau_\lambda} = \frac{1}{N_q}\left[\sum_{\lambda'\lambda''}^{(+)} \Gamma^{(+)}_{\lambda\lambda'\lambda''} + \sum_{\lambda'\lambda''}^{(-)} \frac{1}{2}\Gamma^{(-)}_{\lambda\lambda'\lambda''}\right] + \frac{1}{N}\left[\sum_{\lambda'\lambda''\lambda'''}^{(++)} \frac{1}{2}\Gamma^{(++)}_{\lambda\lambda'\lambda''\lambda'''} + \sum_{\lambda'\lambda''\lambda'''}^{(+-)} \frac{1}{2}\Gamma^{(+-)}_{\lambda\lambda'\lambda''\lambda'''} + \sum_{\lambda'\lambda''\lambda'''}^{(--)} \frac{1}{6}\Gamma^{(--)}_{\lambda\lambda'\lambda''\lambda'''}\right], \tag{3}$$

where N_q denotes the total number of grid points used in the PBTE solution. Superscripts $(\pm)$ and $(\pm\pm)$ differentiate between various 3ph and 4ph scattering mechanisms. The 3ph processes include absorption ($\lambda + \lambda' \rightarrow \lambda''$), where two phonons combine; and emission ($\lambda \rightarrow \lambda' + \lambda''$), where one phonon decays into two. For the higher-order 4ph interactions, there are recombination processes ($\lambda + \lambda' + \lambda'' \rightarrow \lambda'''$), involving the merging of three phonons; redistribution ($\lambda + \lambda' \rightarrow \lambda'' + \lambda'''$), where two phonons are transformed into another pair; and splitting ($\lambda \rightarrow \lambda' + \lambda'' + \lambda'''$), where one phonon splits into three.

Since in this investigation we focus on the effect of anharmonicity on κ in β-Ga_2O_3, it is useful to consider a quantitative measure of anharmonicity. Such a metric allows relating macroscopic properties—here, we focus on thermal transport—to the individual nuclei dynamics. This is further motivated by the complex nature of β-Ga_2O_3 having five nonequivalent atoms in the primitive cell (Fig. 1). Typically,

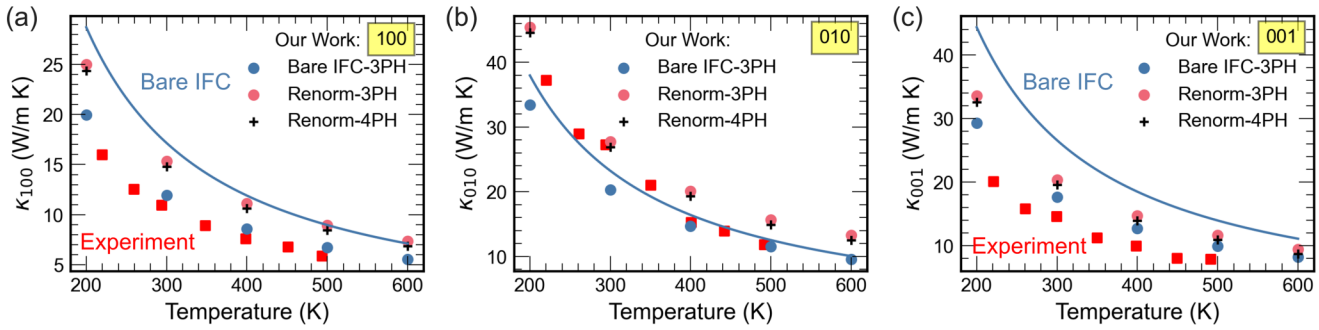

FIG. 2. Plots of the thermal conductivity κ as a function of temperature for three directions: (a) κ_{100}, (b) κ_{010}, and (c) κ_{001}. We include experimental measurements (red squares [8]) and bare interatomic force constant (IFC) calculation fits (blue line [19]) for comparison. For our results, we include κ calculated in different approximations: bare IFC with three-phonon (3ph) scattering (blue symbols), renormalized phonons (Renorm) with 3ph scattering (red symbols), and renormalized phonons with 3ph and four-phonon scattering (black symbols).

anharmonicity is quantified by perturbatively mapping out the ground-state PES of all the unique atom pairs in the crystal structure [58,59]. However, this method is tedious, as the dimensionality of the PES scales with the number of atoms in the unit cell. Furthermore, if we consider that the ground-state PES might not accurately describe the dynamics of nuclei at finite temperatures, then there is no guarantee that anharmonicity quantification using the ground-state PES yields valid results. More recently, Knoop *et al.* [60] derived a measure of anharmonicity (σ_{A}) based on the standard deviation of the average difference between the ground-state harmonic forces and AIMD forces

$$\sigma_{\mathrm{A}}(T) = \sqrt{\frac{\sum_{I\alpha} \left\langle \left[F_{I\alpha} - F_{I\alpha}^{(2)}\right]^2 \right\rangle}{\sum_{I\alpha} \left\langle (F_{I\alpha})^2 \right\rangle}}, \tag{4}$$

where I represents the atom index, and α represents a Cartesian direction. In this paper, we adopt a slightly modified version of their metric. Instead of using ground-state harmonic force constants, we rely on the temperature-dependent (renormalized) IFCs from s-TDEP. This approach allows us to evaluate an effective anharmonicity for each atom in the crystal structure at no additional computational cost. We note that, because TDEP IFCs already include certain anharmonic effects, this represents an effective (rather than purely ground-state) measure of anharmonicity, which is especially useful for systems prone to dynamic instabilities (e.g., showing negative phonon frequencies). Anharmonicity is typically regarded as a material property [60]. Here, we examine how it manifests in very anisotropic materials at the level of individual atoms.

We use VASP 5.4.1 [61–63] for all DFT calculations, FourPhonon [57] for the PBTE solution, and TDEP [49–52] to extract the temperature-dependent IFC. The detailed numerical parameters are discussed in the Appendix. At the time of preparing the manuscript, we became aware of a study on κ in β-Ga_2O_3 including the effect of phonon renormalization using TDEP [64]. However, they showed that including phonon renormalization does not fully resolve underprediction discrepancy for κ_{010}. In this paper, we show otherwise. We attribute this to their much coarser DFT numerical settings. For example, we use a cutoff energy of 640 eV with a $(4 \times 4 \times 4)$ mesh for the supercell, while they use a 400 eV cutoff energy and a $(1 \times 1 \times 1)$ mesh.

III. RESULTS AND DISCUSSION

In Fig. 2, we plot the temperature dependence of the anisotropic thermal conductivity of β-Ga_2O_3 for each of the independent crystal directions. Discrepancies between experiment and theory are evident and can be mitigated with the inclusion of the salient phonon renormalization effects. Predictions of thermal conductivity using the bare IFCs from the literature (blue curve [19]) appreciably overpredict the experimental results (red squares [8]) for κ_{100} and κ_{001}. However, for κ_{010}, the bare IFC prediction is nearly equivalent to experiment over a range of temperatures. It is unclear why defects should affect transport in one direction more than another. Furthermore, since the computational approach presumes no extrinsic defects while actual materials are beset by them, thermal conductivity predictions should be larger than their measured counterparts to some degree. For these reasons, we assert that the directional differences are due to some other factor beyond that of defects.

Figure 2 also includes a summary of our calculated results including 3ph scattering with the bare IFCs, with phonon renormalization, and including 4ph scattering with phonon renormalization (blue, red, and black symbols, respectively). For κ_{100} and κ_{001}, our bare IFC phonon results are lower than the computational results from the literature. Once the effect of phonon normalization is introduced, κ_{100} and κ_{001} increase and are in very good agreement with the bare IFCs κ from the literature. We attribute differences between our bare IFC results and those from the literature mainly to different supercell sizes (160 atoms in this paper vs 80).

For κ_{010}, our bare phonon calculations still anomalously overlap the experimental and computational literature values. However, once we introduce phonon renormalization into the picture, κ_{010} increases and becomes in line with the observations of thermal conductivity in the other directions (i.e., slightly higher than that of the experiment). This resolves the discrepancy between experiment and theory for κ_{010}. Including 4ph scattering has a small ($<5\%$) effect on κ in all directions and across the temperatures considered. This is because the phase space for 3ph processes is huge ($\approx 10^9$ processes). This leads to phonon lifetimes being dominated by 3ph scattering processes rather than the weaker 4ph processes, which typically become dominant if the 3ph phase space is restricted. Therefore, the following discussion probing the

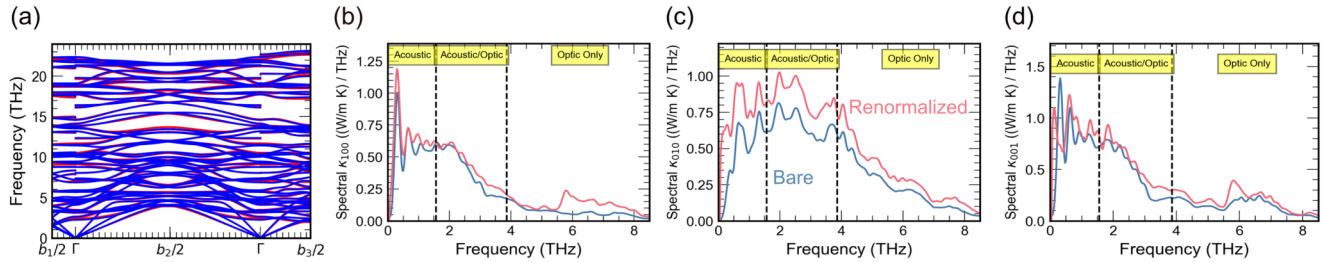

FIG. 3. (a) Phonon dispersion plotted along the three reciprocal lattice vectors for the bare phonon model (blue) and the model including phonon renormalization at 300 K (red). Spectral thermal conductivity for (b) κ_{100}, (c) κ_{010}, and (d) κ_{001} obtained at 300 K using both bare (blue) and renormalized phonons (red). The dashed vertical lines represent the frequency of the lowest optical mode and the highest acoustic mode, respectively.

anisotropic nature of anharmonicity is performed including 3ph scattering only.

Up to this point, we have shown that including phonon renormalization in the computational model resolves the anisotropic discrepancy in κ between theory and experiment. This is a case where anharmonicity manifests itself anisotropically into the material properties. Therefore, anharmonicity is not a binary metric for materials with low symmetry. The importance of this for practical applications cannot be understated. The ability to tune the anharmonicity of a material in a given direction may be crucial in applications where material anisotropy is relevant. For example, κ anisotropy could be leveraged to control heat flow path in electronic systems [65].

Now we turn our attention to understanding the microscopic origins by which phonon renormalization enhances κ along certain directions more than others. As shown in Fig. 3(a), accounting for phonon renormalization results in a slight shift of the phonon mode energies. To further isolate the phonon modes responsible for the κ enhancement, we plot the anisotropic spectral thermal conductivity at 300 K in Figs. 3(b)–3(d) for both the bare IFC and renormalized phonons. We observe that, across all directions, >90% of the κ enhancement is due to phonon modes <8 THz. The spectral functions also show the anisotropic nature of the κ enhancement due to phonon renormalization: 20% for κ_{100}, 29% for κ_{010}, and 17% for κ_{001}. Furthermore, decomposing κ into acoustic and optical phonon contributions—as shown in Figs. 3(b)–3(d)—reveals that both types of modes carry more heat with the inclusion of phonon renormalization. While inclusion of the effect modifies the relative contributions from acoustic and optical modes, the contribution from optical phonon modes to κ remains significant. For example, optical modes are responsible for 48% of the heat transport in κ_{010}. This high optical phonon contribution is common in complex materials with significant κ anisotropy [66–69].

Since we are dealing with bulk solids, phonon modes carry more heat either because of an increase in the group velocity or a decrease in the phonon scattering rate. Therefore, we investigate the changes in group velocity and lifetimes of the relevant phonon modes in an attempt to answer two questions: Why does κ increase when including phonon renormalization in the computational model, and why is this increase anisotropic?

In Fig. 4(a), we plot the phonon lifetimes at 300 K for both the bare IFC (blue) and renormalized (red) phonons. We notice that the phonon lifetimes increase across the relevant phonon frequency range (0–8 THz). This is the origin of the observed κ enhancement. Differences in the phonon lifetimes stem from either a change in the number of phonon scattering events that obey the energy and momentum conservation (i.e., phase space) or the higher-order IFCs. In Fig. 4(b), we compare the weighted phase space from both models. The weighted phase space represents the number of phonon interactions that obey energy and momentum conservation scaled

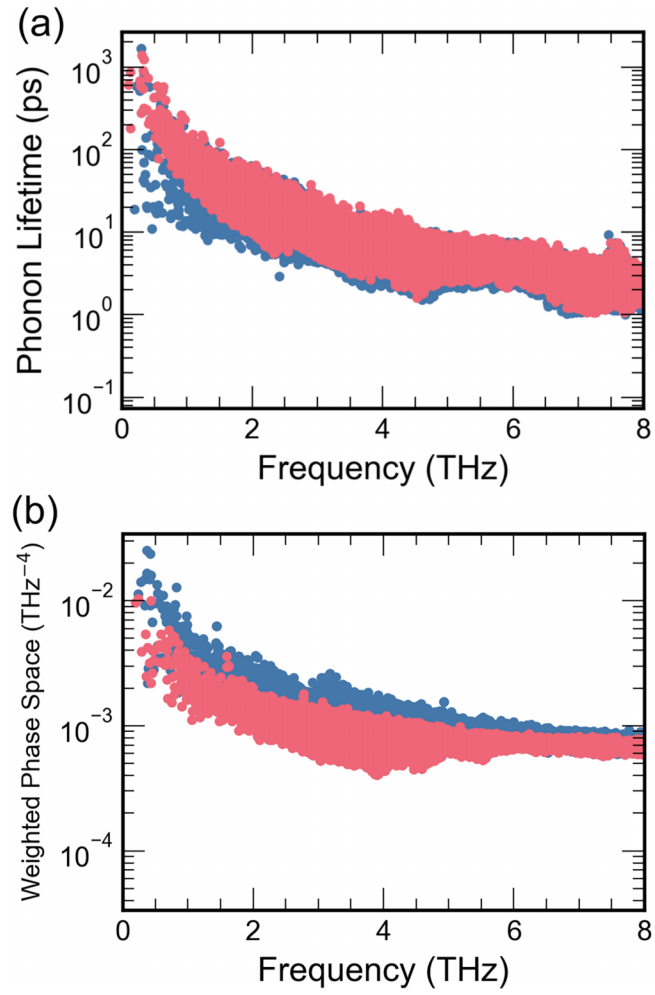

FIG. 4. (a) Phonon lifetimes and (b) weighted phase-space at 300 K for the bare interatomic force constant (IFC) phonon model (blue) and the model including phonon renormalization at 300 K (red).

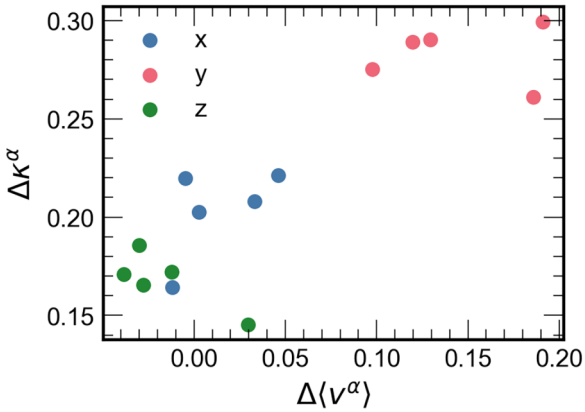

FIG. 5. Scatter plot of the relative change in thermal conductivity ($\Delta\kappa^\alpha$) against the relative change in the heat-averaged group velocity ($\Delta\langle v^\alpha\rangle$) for the three Cartesian directions: x (blue), y (red), and z (green) for all studied temperatures (200–600 K). Note that the x and y directions correspond to the (100) and (010) directions, respectively. However, the z direction does not correspond to a lattice vector owing to the nonorthogonal nature of the crystal. See the Appendix for more detail.

by the occupation factors and normalized by the phonon frequencies. As a result, the weighted phase space is much more sensitive to phonon frequency shifts than the phase space alone (order x^5 vs order x) [70]. It is clear that the weighted phase space for the renormalized phonons is smaller than that of the bare phonons. This provides a clear answer to our first question. Accounting for phonon renormalization boosts κ as a result of longer phonon lifetimes due to a more restricted phonon phase space.

To address the anisotropic κ enhancement, we need to analyze the phonon group velocity, as it is the only parameter in the κ expression [Eq. (1)] that has directional components. For this purpose, we define a heat-averaged group velocity $\langle v^\alpha\rangle$:

$$\langle v^\alpha\rangle = \frac{\sum_\lambda \kappa_\lambda^\alpha |v_\lambda^\alpha|}{\sum_\lambda \kappa_\lambda^\alpha}, \tag{5}$$

where α represents the Cartesian direction, and λ is the mode index. This metric allows us to meaningfully link changes in the group velocity to changes in κ. The difference between the thermal conductivity in the direction of the lattice vectors (κ_{010}) and that in the Cartesian direction (κ_{zz}) is discussed in the Appendix. In Fig. 5, we plot the relative change in κ^α against the relative change in $\langle v^\alpha\rangle$. We observe that there is clear correspondence between the change in $\langle v^\alpha\rangle$ and the anisotropic κ enhancement. The largest relative κ increase is in the y direction, which also has the largest relative change in $\langle v^\alpha\rangle$. Furthermore, the lowest κ increase is in the z direction, which has a slight decrease in $\langle v^\alpha\rangle$. The emergence of outliers is likely due to the nontrivial shifts in the phonon energies due to phonon renormalization. The consistent observation of this trend across all studied temperatures underscores the generality of our analysis. This answers our second question—why is the increase in thermal conductivity anisotropic when accounting for phonon renormalization? With both questions addressed, the results are fully explained in the framework of the phonon gas model. Having demonstrated the importance of accounting for anharmonicity in the phonon energies, we now turn our attention to addressing the anharmonicity of the atoms in real space, with an attempt to link it to the κ increase due to phonon renormalization.

Following the modified anharmonicity metric of Knoop *et al.* [60], we plot the temperature dependence of the mean anharmonicity for all unique atoms in β-Ga_2O_3 [Fig. 6(a)]. Although the mean anharmonicity at 300 K of β-Ga_2O_3 (0.21) is only slightly higher than that of silicon (0.15) [25], examining the anharmonicity of the individual atoms reveals important physics. Most importantly, we observe that the octahedrally coordinated Ga_{II} (see Fig. 1) is the most anharmonic atom across the studied temperature range. We also plot the atom-projected phonon density of states (PDOS) at 300 K for bare [Fig. 6(b)] and renormalized [Fig. 6(c)] phonons. It is clear that Ga_{II} also peaks and has the highest PDOS contribution in the phonon frequency range where the κ enhancement occurs (0–8 THz). The Ga_{II} contribution to the PDOS even increases slightly when we account for phonon renormalization. This strongly suggests that the κ increase is directly related to the dynamics of the Ga_{II} nuclei. This reveals the origin of the failure of the harmonic approximation to accurately predict the anisotropic κ in β-Ga_2O_3. Therefore, it can be argued that including phonon renormalization in the computational model leads to an increase in κ because it has a more accurate description of the dynamics of the Ga_{II} nuclei.

By examining the anharmonicity of the individual atoms in β-Ga_2O_3, we notice that atoms of the same element have significantly different anharmonicities. We focus on tetrahedrally coordinated Ga and octahedrally coordinated Ga_{II}, as they have the highest contribution in the PDOS range of interest (0–8 THz). The fact that Ga_I has lower anharmonicity than Ga_{II} is in line with results obtained by Xia *et al.* [33]. In their study, they calculate κ of a wide range of binary rocksalt (octahedral coordination) and zinc-blende (tetrahedral coordination) materials. They discovered that, regardless of the κ of a material, rocksalt materials have a stronger response (larger κ increase) to phonon renormalization than zinc-blende materials. However, due to the complex structure of β-Ga_2O_3, gallium atoms with both coordinations exist. Therefore, what we reveal in this paper about the link between atom anharmonicity, coordination, and phonon renormalization has been shown before, albeit for materials that have only a single coordination in their structure. In the final part of this paper, we demonstrate how an analysis of atomic anharmonicity could be used to tailor vibrational properties in complex structures.

The higher anharmonicity of Ga_{II} relative to Ga_I opens up an interesting question: What if we replace Ga_{II} with another atom with lower anharmonicity with the purpose of increasing κ? In his seminal work, Slack [71] proposes four rules for finding materials with higher thermal conductivity: low atomic mass, strong bonding, simple crystal structure, and low anharmonicity. Therefore, it would be reasonable to replace Ga_{II} with boron, the lightest element in group III. However, it has been shown that it is thermodynamically favorable for boron to occupy the Ga_I site [72]. The second-lightest atom in the group is aluminum. Substituting in aluminum, which preferentially occupies the Ga_{II} site, to create a structured β-$AlGaO_3$ alloy has been shown to increase the mean κ by

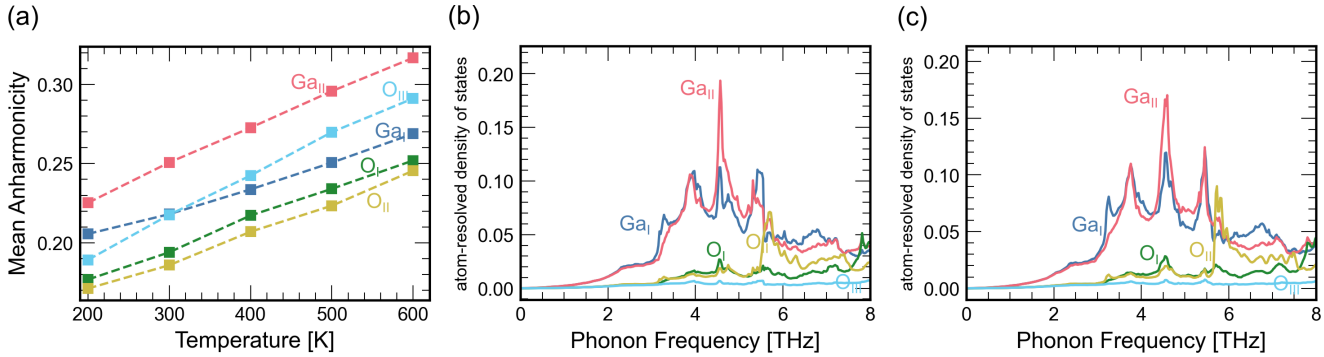

FIG. 6. Temperature-dependence of (a) the nonequivalent-atom anharmonicity and (b) the atom-resolved phonon density of states at 300 K for the bare interatomic force constant (IFC) and (c) renormalized phonons.

>70% [73]. Here, we have demonstrated that using Slack's rule to lower the atomic masses, atom anharmonicity to decide on which element to replace and thermodynamics to understand preferential occupation sites provides a rational design process that enables tailoring the vibrational properties of complex materials. A comprehensive study to tune the thermal transport or optical response in β-Ga_2O_3 or other complex structures is the subject of a future study.

IV. CONCLUSIONS

To conclude, using DFT coupled with a solution of the PBTE, we resolve the inconsistency between experimental results and computational models for κ in β-Ga_2O_3. Our findings reveal that phonon renormalization increases κ anisotropically. This anisotropic enhancement is attributed to phonons with longer lifetimes due to a more restricted phase space and anisotropic changes in phonon group velocities. Moreover, in our investigation into the anharmonicity of atoms, we identified the octahedrally coordinated gallium atom as the most anharmonic, likely causing the failure of the harmonic phonon model in β-Ga_2O_3. We also gave insights that atomic anharmonicities could serve as a valuable metric for tuning the vibrational properties of materials. These insights provide a pathway for optimizing thermal and optical properties in β-Ga_2O_3 and other complex materials.

ACKNOWLEDGMENTS

A.A. acknowledges financial support from Kuwait University. Z.H., Z.G., and X.R. acknowledge partial support from U.S. National Science Foundation Awards No. 2311848 and No. 2321301. A.A. thanks Olle Hellman for providing access to TDEP and Florian Knoop at Linköping University for TDEP assistance and valuable discussions.

APPENDIX: NUMERICAL PARAMETERS AND DETAILS

For DFT simulations, we use VASP 5.4.1 [61–63,74,75]. All calculations were carried out using the PBEsol [76] exchange-correlation functional with the projector augmented-wave method for the pseudopotentials. The valence electron configurations include $3d^{10}\,4s^2\,4p^1$ for Ga and $2s^2\,2p^4$ for O. For the structural relaxation, we use a cutoff energy of 640 eV, an energy convergence threshold of 10^{-8} eV, a force convergence threshold of 10^{-7} eV/Å, and a Γ-centered **k**-point mesh of $4 \times 16 \times 8$. Using these settings, we obtain a relaxed conventional unit cell with $a = 12.269$ Å, $b = 3.048$ Å, $c = 5.810$ Å, and $\beta = 103.78°$. These are in good agreement with experimental results ($a = 12.214$ Å, $b = 3.0371$ Å, $c = 5.7981$ Å, and $\beta = 103.83°$) [13].

For the harmonic phonon calculations, we use the DFPT module in VASP (on a $4 \times 4 \times 4$ mesh) with PHONOPY [77,78] to calculate the phonon dispersion for a $1 \times 4 \times 2$ supercell (160 atoms). For the polar correction, we also calculate the Born effective charges and dielectric tensor for the unit cell using the DFPT module in VASP. The higher-order IFCs were calculated using the finite-displacement method as implemented in ShengBTE [48,79,80] and its FourPhonon [57] extension package with the default displacement value (0.01 Å). For the third- and fourth-order IFCs, we use the 11th-nearest neighbor (3.5 Å) and second-nearest neighbor (2.38 Å) cutoffs, respectively.

For the renormalized phonons, we construct a $1 \times 4 \times 2$ supercell from the relaxed unit cell which is expanded using the experimental value of the linear thermal [81] expansion at each temperature. Following this, we generate an initial guess of the phonon dispersion based on the Debye temperature (738 K) [8]. Thermally excited supercells are then generated from the normal modes based on a Bose-Einstein distribution. A new set IFCs is obtained for each temperature from these thermal snapshots, and the process is repeated until a self-consistent solution is achieved. This method is described in detail in Ref. [53]. We use the same IFC cutoffs used for the harmonic phonons, and we consider the IFCs converged when the thermal conductivity changes by <2%. To achieve this, we generate 200 configurations twice, followed by 400 configurations twice, without mixing the IFCs. In hindsight, we would not recommend such a process, as it is computationally wasteful and could lead to oscillatory convergence. A more reasonable approach would be to use a geometric series with mixing of the IFCs as described in Ref. [53]. Further expanding on this matter, we tested the two workflows for iteratively determining the IFCs: one that mixes IFCs between successive steps and one that does not. We find that both approaches lead to final thermal conductivity values that agree within 2%, indicating no significant difference in accuracy.

However, adopting an IFC mixing scheme generally requires fewer iterations and DFT calculations to reach convergence.

To calculate the thermal conductivity, we use the ShengBTE extension package FourPhonon on a $10 \times 40 \times 20$ mesh. We also calculate the thermal conductivity under the relaxed-time approximation (RTA). The difference between the RTA and the full iterative solution is $<2\%$. For 4ph scattering, we adopt a sampling-based approach. In this method, the 4ph scattering rates are determined from a subset of all phonon scattering events as described in Ref. [82]. Following a convergence test, we use a sampling size of 8×10^7.

Since the lattice vectors of β-Ga_2O_3 are not orthogonal, we need to convert the computational thermal conductivity tensor (obtained in Cartesian coordinates) to a tensor that is in the basis of the lattice vectors. This will enable us to compare our results to experimental values. For κ_{100} and κ_{010}, these directions are parallel to the Cartesian axes (i.e., $\kappa_{100} = \kappa_{xx}$ and $\kappa_{010} = \kappa_{yy}$). However, this is not the case for κ_{001}, which has components in the x and z directions. Therefore, we calculate κ_{001} from the Cartesian tensor as follows [19]:

$$\kappa_{001} = \kappa_{xx} \sin^2(\beta) + \kappa_{xz} \sin(2\beta) + \kappa_{zz} \cos^2(\beta). \quad \text{(A1)}$$

[1] J. Y. Tsao *et al.*, Ultrawide-bandgap semiconductors: Research opportunities and challenges, Adv. Electron. Mater. **4**, 1600501 (2018).

[2] M. H. Wong, O. Bierwagen, R. J. Kaplar, and H. Umezawa, Ultrawide-bandgap semiconductors: An overview, J. Mater. Res. **36**, 4601 (2021).

[3] T. E. Beechem, A. E. McDonald, E. J. Fuller, A. A. Talin, C. M. Rost, J.-P. Maria, J. T. Gaskins, P. E. Hopkins, and A. A. Allerman, Size dictated thermal conductivity of GaN, J. Appl. Phys. **120**, 095104 (2016).

[4] Y. Song, C. Perez, G. Esteves, J. S. Lundh, C. B. Saltonstall, T. E. Beechem, J. I. Yang, K. Ferri, J. E. Brown, Z. Tang *et al.*, Thermal conductivity of aluminum scandium nitride for 5G mobile applications and beyond, ACS Appl. Mater. Interfaces **13**, 19031 (2021).

[5] K. Sasaki, M. Higashiwaki, A. Kuramata, T. Masui, and S. Yamakoshi, MBE grown Ga_2O_3 and its power device applications, J. Cryst. Growth **378**, 591 (2013).

[6] M. Higashiwaki, K. Sasaki, A. Kuramata, T. Masui, and S. Yamakoshi, Development of gallium oxide power devices, Phys. Status Solidi A **211**, 21 (2014).

[7] S. B. Reese, T. Remo, J. Green, and A. Zakutayev, How much will gallium oxide power electronics cost? Joule **3**, 903 (2019).

[8] Z. Guo, A. Verma, X. Wu, F. Sun, A. Hickman, T. Masui, A. Kuramata, M. Higashiwaki, D. Jena, and T. Luo, Anisotropic thermal conductivity in single crystal β-gallium oxide, Appl. Phys. Lett. **106**, 111909 (2015).

[9] Z. Cheng, J. Liang, K. Kawamura, H. Zhou, H. Asamura, H. Uratani, J. Tiwari, S. Graham, Y. Ohno, Y. Nagai *et al.*, High thermal conductivity in wafer-scale cubic silicon carbide crystals, Nat. Commun. **13**, 7201 (2022).

[10] C. Mion, J. F. Muth, E. A. Preble, and D. Hanser, Accurate dependence of gallium nitride thermal conductivity on dislocation density, Appl. Phys. Lett. **89**, 092123 (2006).

[11] K. Kim, W. Hwang, S.-H. V. Oh, and A. Soon, Exploring anharmonic lattice dynamics and dielectric relations in niobate perovskites from first-principles self-consistent phonon calculations, npj Comput. Mater. **9**, 154 (2023).

[12] R. E. Newnham, *Properties of Materials Anisotropy, Symmetry, Structure*, Oxford Scholarship Online (Oxford University Press, Oxford, 2005).

[13] J. Åhman, G. Svensson, and J. Albertsson, A reinvestigation of β-gallium oxide, Acta Crystallogr. Sect. C **52**, 1336 (1996).

[14] M. Handwerg, R. Mitdank, Z. Galazka, and S. F. Fischer, Temperature-dependent thermal conductivity and diffusivity of a Mg-doped insulating β-Ga_2O_3 single crystal along [100], [010] and [001], Semicond. Sci. Technol. **31**, 125006 (2016).

[15] P. Jiang, X. Qian, X. Li, and R. Yang, Three-dimensional anisotropic thermal conductivity tensor of single crystalline β-Ga_2O_3, Appl. Phys. Lett. **113**, 232105 (2018).

[16] M. Slomski, N. Blumenschein, P. P. Paskov, J. F. Muth, and T. Paskova, Anisotropic thermal conductivity of β-Ga_2O_3 at elevated temperatures: Effect of Sn and Fe dopants, J. Appl. Phys. **121**, 235104 (2017).

[17] D. Klimm, B. Amgalan, S. Ganschow, A. Kwasniewski, Z. Galazka, and M. Bickermann, The thermal conductivity tensor of β-Ga_2O_3 from 300 to 1275 K, Cryst. Res. Technol. **58**, 2200204 (2023).

[18] L. Lindsay, D. A. Broido, and T. L. Reinecke, Thermal conductivity and large isotope effect in GaN from first principles, Phys. Rev. Lett. **109**, 095901 (2012).

[19] M. D. Santia, N. Tandon, and J. D. Albrecht, Lattice thermal conductivity in β-Ga_2O_3 from first principles, Appl. Phys. Lett. **107**, 041907 (2015).

[20] Z. Yan and S. Kumar, Phonon mode contributions to thermal conductivity of pristine and defective β-Ga_2O_3, Phys. Chem. Chem. Phys. **20**, 29236 (2018).

[21] L. Lindsay, A. Katre, A. Cepellotti, and N. Mingo, Perspective on *ab initio* phonon thermal transport, J. Appl. Phys. **126**, 050902 (2019).

[22] A. J. H. McGaughey, A. Jain, and H.-Y. Kim, Phonon properties and thermal conductivity from first principles, lattice dynamics, and the Boltzmann transport equation, J. Appl. Phys. **125**, 011101 (2019).

[23] M. Simoncelli, N. Marzari, and F. Mauri, Wigner formulation of thermal transport in solids, Phys. Rev. X **12**, 041011 (2022).

[24] M. Schubert, R. Korlacki, S. Knight, T. Hofmann, S. Schöche, V. Darakchieva, E. Janzén, B. Monemar, D. Gogova, Q.-T. Thieu *et al.*, Anisotropy, phonon modes, and free charge carrier parameters in monoclinic β-gallium oxide single crystals, Phys. Rev. B **93**, 125209 (2016).

[25] F. Knoop, T. A. R. Purcell, M. Scheffler, and C. Carbogno, Anharmonicity in thermal insulators: An analysis from first principles, Phys. Rev. Lett. **130**, 236301 (2023).

[26] L. Isaeva, G. Barbalinardo, D. Donadio, and S. Baroni, Modeling heat transport in crystals and glasses from a unified lattice-dynamical approach, Nat. Commun. **10**, 3853 (2019).

[27] M. Simoncelli, N. Marzari, and F. Mauri, Unified theory of thermal transport in crystals and glasses, Nat. Phys. **15**, 809 (2019).

[28] D. Tisi, F. Grasselli, L. Gigli, and M. Ceriotti, Thermal conductivity of Li_3PS_4 solid electrolytes with *ab initio* accuracy, Phys. Rev. Mater. **8**, 065403 (2024).

[29] A. Pazhedath, L. Bastonero, N. Marzari, and M. Simoncelli, First-principles characterization of thermal conductivity in $LaPO_4$-based alloys, Phys. Rev. Appl. **22**, 024064 (2024).

[30] K. Pal, Y. Xia, and C. Wolverton, Microscopic mechanism of unusual lattice thermal transport in $TlInTe_2$, npj Comput. Mater. **7**, 5 (2021).

[31] Q.-Y. Xie, P.-F. Liu, J.-J. Ma, L.-M. Wu, K.-W. Zhang, and B.-T. Wang, Microscopic mechanisms of glasslike lattice thermal conductivity in tetragonal α-$CsCu_5Se_3$, Phys. Rev. B **108**, 014302 (2023).

[32] Z. Zeng, C. Zhang, Y. Xia, Z. Fan, C. Wolverton, and Y. Chen, Nonperturbative phonon scatterings and two-channel thermal transport in Tl_3VSe_4, Phys. Rev. B **103**, 224307 (2021).

[33] Y. Xia, V. I. Hegde, K. Pal, X. Hua, D. Gaines, S. Patel, J. He, M. Aykol, and C. Wolverton, High-throughput study of lattice thermal conductivity in binary rocksalt and zinc blende compounds including higher-order anharmonicity, Phys. Rev. X **10**, 041029 (2020).

[34] Z. Tong, A. Pecchia, C. Yam, T. Dumitrică, and T. Frauenheim, Glasslike transport dominates ultralow lattice thermal conductivity in modular crystalline $Bi_4O_4SeCl_2$, Nano Lett. **23**, 9468 (2023).

[35] R. M. Martin, *Electronic Structure: Basic Theory and Practical Methods* (Cambridge University Press, Cambridge, 2004).

[36] S. Baroni, S. de Gironcoli, A. Dal Corso, and P. Giannozzi, Phonons and related crystal properties from density-functional perturbation theory, Rev. Mod. Phys. **73**, 515 (2001).

[37] N. K. Ravichandran and D. Broido, Unified first-principles theory of thermal properties of insulators, Phys. Rev. B **98**, 085205 (2018).

[38] Z. Han and X. Ruan, Thermal conductivity of monolayer graphene: Convergent and lower than diamond, Phys. Rev. B **108**, L121412 (2023).

[39] A. H. Romero, E. K. U. Gross, M. J. Verstraete, and O. Hellman, Thermal conductivity in PbTe from first principles, Phys. Rev. B **91**, 214310 (2015).

[40] B. Fu, G. Tang, and A. J. H. McGaughey, Finite-temperature force constants are essential for accurately predicting the thermal conductivity of rutile TiO_2, Phys. Rev. Mater. **6**, 015401 (2022).

[41] T. Guo and D. Guo, Anharmonic phonon renormalization and two-channel thermal transport in $SrTiO_3$ using full temperature-dependent interatomic force constant, Phys. Lett. A **467**, 128727 (2023).

[42] T. Feng and X. Ruan, Quantum mechanical prediction of four-phonon scattering rates and reduced thermal conductivity of solids, Phys. Rev. B **93**, 045202 (2016).

[43] T. Feng, L. Lindsay, and X. Ruan, Four-phonon scattering significantly reduces intrinsic thermal conductivity of solids, Phys. Rev. B **96**, 161201(R) (2017).

[44] X. Yang, T. Feng, J. Li, and X. Ruan, Stronger role of four-phonon scattering than three-phonon scattering in thermal conductivity of III-V semiconductors at room temperature, Phys. Rev. B **100**, 245203 (2019).

[45] X.-K. Chen, E.-M. Zhang, D. Wu, and K.-Q. Chen, Strain-induced medium-temperature thermoelectric performance of Cu_4TiSe_4: The role of four-phonon scattering, Phys. Rev. Appl. **19**, 044052 (2023).

[46] Z. Guo, Z. Han, A. Alkandari, K. Khot, and X. Ruan, First-principles prediction of thermal conductivity of bulk hexagonal boron nitride, Appl. Phys. Lett. **124**, 163906 (2024).

[47] M. A. Huque, L. M. Tolbert, B. J. Blalock, and S. K. Islam, A high-temperature, high-voltage SOI gate driver IC with high output current and on-chip low-power temperature sensor, IMPAS International Symposium on Microelectronics (2009), pp. 220–227.

[48] W. Li and N. Mingo, Lattice dynamics and thermal conductivity of skutterudites $CoSb_3$ and $IrSb_3$ from first principles: Why $IrSb_3$ is a better thermal conductor than $CoSb_3$, Phys. Rev. B **90**, 094302 (2014).

[49] O. Hellman, P. Steneteg, I. A. Abrikosov, and S. I. Simak, Temperature dependent effective potential method for accurate free energy calculations of solids, Phys. Rev. B **87**, 104111 (2013).

[50] O. Hellman and I. A. Abrikosov, Temperature-dependent effective third-order interatomic force constants from first principles, Phys. Rev. B **88**, 144301 (2013).

[51] O. Hellman, I. A. Abrikosov, and S. I. Simak, Lattice dynamics of anharmonic solids from first principles, Phys. Rev. B **84**, 180301(R) (2011).

[52] F. Knoop, N. Shulumba, A. Castellano, J. P. A. Batista, R. Farris, M. J. Verstraete, M. Heine, D. Broido, D. S. Kim, J. Klarbring *et al.*, TDEP: Temperature dependent effective potentials, J. Open Source Software **9**, 6150 (2024).

[53] N. Shulumba, O. Hellman, and A. J. Minnich, Intrinsic localized mode and low thermal conductivity of PbSe, Phys. Rev. B **95**, 014302 (2017).

[54] Y. Xia, Revisiting lattice thermal transport in PbTe: The crucial role of quartic anharmonicity, Appl. Phys. Lett. **113**, 073901 (2018).

[55] N. Benshalom, G. Reuveni, R. Korobko, O. Yaffe, and O. Hellman, Dielectric response of rock-salt crystals at finite temperatures from first principles, Phys. Rev. Mater. **6**, 033607 (2022).

[56] J. M. Ziman, *Electrons and Phonons: The Theory of Transport Phenomena in Solids*, Oxford Classic Texts in the Physical Sciences (Oxford University Press, Oxford, 2001).

[57] Z. Han, X. Yang, W. Li, T. Feng, and X. Ruan, Four-Phonon: An extension module to ShengBTE for computing four-phonon scattering rates and thermal conductivity, Comput. Phys. Commun. **270**, 108179 (2022).

[58] S.-Y. Yue, X. Zhang, G. Qin, S. R. Phillpot, and M. Hu, Metric for strong intrinsic fourth-order phonon anharmonicity, Phys. Rev. B **95**, 195203 (2017).

[59] P. Wu, K. Xia, K. Peng, T. Honda, K. Ikeda, F. Liu, P. Vallobra, F. Fan, J. Song, D. Zhang *et al.*, Strong anharmonicity in tin monosulfide evidenced by local distortion, high-energy optical phonons, and anharmonic potential, Phys. Rev. B **103**, 195204 (2021).

[60] F. Knoop, T. A. R. Purcell, M. Scheffler, and C. Carbogno, Anharmonicity measure for materials, Phys. Rev. Mater. **4**, 083809 (2020).

[61] G. Kresse and J. Hafner, *Ab Initio* molecular dynamics for liquid metals, Phys. Rev. B **47**, 558 (1993).

[62] G. Kresse and J. Furthmüller, Efficiency of *ab-initio* total energy calculations for metals and semiconductors using a plane-wave basis set, Comput. Mater. Sci. **6**, 15 (1996).

[63] G. Kresse and J. Furthmüller, Efficient iterative schemes for *ab initio* total-energy calculations using a plane-wave basis set, Phys. Rev. B **54**, 11169 (1996).

[64] Y. Chen, L. Peng, Y. Wu, C. Ma, A. Wu, H. Zhang, and Z. Fang, Anomalous temperature-dependent phonon anharmonicity and strain engineering of thermal conductivity in β-Ga_2O_3, J. Phys. Chem. C, **127**, 13356 (2023).

[65] E. M. Dede, Simulation and optimization of heat flow via anisotropic material thermal conductivity, Comput. Mater. Sci. **50**, 510 (2010).

[66] S. Mukhopadhyay, L. Lindsay, and D. J. Singh, Optic phonons and anisotropic thermal conductivity in hexagonal $Ge_2Sb_2Te_5$, Sci. Rep. **6**, 37076 (2016).

[67] Z. Li, D. Shi, J. Yang, W. Luo, C. Wan, and W. Pan, Contribution of optical phonons to lattice thermal conductivity in complex structural thermal insulation materials, J. Eur. Ceram. Soc. **41**, 7981 (2021).

[68] Z. Li, H. Xie, S. Hao, Y. Xia, X. Su, M. G. Kanatzidis, C. Wolverton, and X. Tang, Optical phonon dominated heat transport: A first-principles thermal conductivity study of $BaSnS_2$, Phys. Rev. B **104**, 245209 (2021).

[69] T. Pandey, M.-H. Du, D. S. Parker, and L. Lindsay, Origin of ultralow phonon transport and strong anharmonicity in lead-free halide perovskites, Mater. Today Phys. **28**, 100881 (2022).

[70] W. Li, J. Carrete, N. A. Katcho, and N. Mingo, ShengBTE: A solver of the Boltzmann transport equation for phonons, Comput. Phys. Commun. **185**, 1747 (2014).

[71] G. A. Slack, Nonmetallic crystals with high thermal conductivity, J. Phys. Chem. Solids **34**, 321 (1973).

[72] J. Lehtomäki, J. Li, and P. Rinke, Boron doping in gallium oxide from first principles, J. Phys. Commun. **4**, 125001 (2020).

[73] S. Mu, H. Peelaers, and C. G. Van De Walle, *Ab initio* study of enhanced thermal conductivity in ordered $AlGaO_3$ alloys, Appl. Phys. Lett. **115**, 242103 (2019).

[74] G. Kresse and J. Hafner, *Ab initio* molecular-dynamics simulation of the liquid-metal–amorphous-semiconductor transition in germanium, Phys. Rev. B **49**, 14251 (1994).

[75] G. Kresse and D. Joubert, From ultrasoft pseudopotentials to the projector augmented-wave method, Phys. Rev. B **59**, 1758 (1999).

[76] J. P. Perdew, A. Ruzsinszky, G. I. Csonka, O. A. Vydrov, G. E. Scuseria, L. A. Constantin, X. Zhou, and K. Burke, Restoring the density-gradient expansion for exchange in solids and surfaces, Phys. Rev. Lett. **100**, 136406 (2008).

[77] A. Togo, L. Chaput, T. Tadano, and I. Tanaka, Implementation strategies in phonopy and phono3py, J. Phys.: Condens. Matter **35**, 353001 (2023).

[78] A. Togo, First-principles phonon calculations with phonopy and phono3py, J. Phys. Soc. Jpn. **92**, 012001 (2023).

[79] W. Li, L. Lindsay, D. A. Broido, D. A. Stewart, and N. Mingo, Thermal conductivity of bulk and nanowire $Mg_2Si_xSn_{1-x}$ alloys from first principles, Phys. Rev. B **86**, 174307 (2012).

[80] W. Li, N. Mingo, L. Lindsay, D. A. Broido, D. A. Stewart, and N. A. Katcho, Thermal conductivity of diamond nanowires from first principles, Phys. Rev. B **85**, 195436 (2012).

[81] M. E. Liao, C. Li, H. M. Yu, E. Rosker, M. J. Tadjer, K. D. Hobart, and M. S. Goorsky, Coefficients of thermal expansion of single crystalline β-Ga_2O_3 and in-plane thermal strain calculations of various materials combinations with β-Ga_2O_3, APL Mater. **7**, 022517 (2019).

[82] Z. Guo, Z. Han, D. Feng, G. Lin, and X. Ruan, Sampling-accelerated prediction of phonon scattering rates for converged thermal conductivity and radiative properties, npj Comput. Mater. **10**, 31 (2024).